LAWRENCE
LIVERMORE
NATIONAL
LABORATORY

LLNL-JRNL-814145

Method for system-independent materail characterization from spectral x-ray CT

M. Busi, K. A. Mohan, A. A. Dooraghi, K. M. Champley, H. E. Martz, U. L. Olsen

September 1, 2020

Science Direct

Disclaimer

Method for System-Independent Material Characterization from Spectral X-ray CT

Matteo Busi[a,b], K. Aditya Mohan[b], Alex A. Dooraghi[b], Kyle M. Champley[b], Harry E. Martz[b], Ulrik L. Olsen[a]

[a] *Technical University of Denmark, DTU Physics, 2800 Kgs. Lyngby, Denmark*
[b] *Lawrence Livermore National Laboratory, Livermore, CA 94551, USA*

Abstract

We propose a method for material characterization using Spectral X-ray Computed Tomography (SCT). Our SCT method takes advantage of recently-developed MultiX ME 100 photon counting detectors to simultaneously measure the energy dependence of a material's linear attenuation coefficient (LAC). Relative electron density (ρ_e) and effective atomic number (Z_e) are estimated directly from the energy-dependent LAC measurements. The method employs a spectral correction algorithm and automated selection and weighting of the energy bins for optimized performance. When examining materials with $Z_e \leq 23$, this method achieves accuracy comparable to traditional dual-energy CT, which is often realized through consecutive data acquisitions, and is compatible with any spectral detector. The method disregards data in photon starved energy channels improving the detection of highly attenuating materials, compared to techniques that use energy integrating detectors.

Keywords: Spectral X-ray CT, Quantitative X-ray characterization, Effective atomic number, Electron density, Photon Counting Detectors, Security screening

1. Introduction

Laboratory or industrial based X-ray radiography and Computed Tomography (CT) provide structural images of an object (airline baggage, human body, etc.), but do not typically measure quantitative material properties such as electron density or effective atomic number[1, 2]. One reason is because the polychromatic nature of the incident X-rays obscures quantification due to non-linearities in how the radiation is attenuated. Moreover, analysis using the effective linear attenuation coefficient (LAC) to classify materials may result in a system-dependent solution [3]. Recently, a method was presented for material characterization using dual-energy computed tomography (DECT), called System Independent ρ_e/Z_e (SIRZ)[4], which demonstrated accurate and precise results for a set of materials with Z_e between 6 and 20. The results were shown to be consistent between different DECT systems used to perform the acquisitions. However, this method requires collection of two distinct datasets, and includes a set of reference materials for calibration of the detector's spectral response.

Email address: mbusi@fysik.dtu.dk; Fysikvej 307 R251, 2800 Kgs. Lyngby, Denmark (Matteo Busi)

Advances in cadmium telluride (CdTe) energy-discriminating pixelated detectors have enabled the possibility of Spectral X-ray Computed Tomography (SCT) which incorporates spectroscopic information into CT. Theoretical and experimental studies examining photon counting detectors (PCDs) have suggested that SCT outperforms conventional energy-integrating CT in material discrimination and detection tasks[5, 6, 7, 8, 9, 10]. MultiX ME100 (MultiX, Neuilly-sur-Seine, France) is a PCD that has been shown to be able to efficiently handle photon fluxes up to 7 Mphotons/pixel[10], making it a suitable candidate for real scanning applications. Brambilla et al. presented a basis material decomposition method using MultiX ME100 PCD[11]. The method requires a calibration step in which a set of reference material (polyethylene and polyvinyl chloride) is measured. The scanned objects are characterized into thicknesses relative to the reference materials. From these, the effective atomic number, Z_e, of the unknown materials is interpolated or extrapolated. In this work, we present a new method for the estimation of system independent material features (ρ_e and Z_e) from SCT acquisitions. The method estimates material features directly from measured energy resolved LACs. The formulation of the method makes it compatible with an arbitrary number of energy bins.

2. Materials and Methods

In this section, we define the system-independent physical properties we have used to characterize materials. We then describe the instrumentation and the samples used to conduct the experiments. Lastly, we present the algorithm to estimate the system independent features from experimental data.

2.1. Physical properties of materials under investigation

The interactions between photons with energy $E < 1.022$ MeV and a single element with atomic number Z are described in terms of total mass attenuation cross section, $\sigma(Z, E)$ (cm^2/g), which consists of contribution from the photoelectric absorption (σ_{abs}), coherent scattering (σ_{coh}), and incoherent scattering (σ_{inc}) [12]. An illustration of the relative contribution of each component of the mass attenuation cross sections as a function of energy is shown in Fig 1. Note that for the elements commonly found in organic compounds (C, H, N, O), the photoelectric absorption is the dominant contribution for energies below 60 keV; however, the photo-electric absorption increases with Z_e. Also at energies below 60 keV coherent (Rayleigh) scattering is present and accounts for a contribution to the total attenuation of approximately 10%. Above these energies, incoherent (Compton) scattering becomes predominant. We convert total mass cross section into *electronic* cross section ($\mathrm{cm}^2/\mathrm{e}^-\mathrm{mol}$), as:

$$\sigma_e(Z, E) = \frac{A(Z)}{Z}\sigma(Z, E), \tag{1}$$

where $A(Z)$ is the atomic mass (g/mole) of the element Z. Likewise, we convert the bulk density ρ (g/cm^3) into *electron* density ρ_e ($\mathrm{e}^-\mathrm{mol}/\mathrm{cm}^3$), using the relation:

$$\rho_e = \frac{Z}{A(Z)}\rho. \tag{2}$$

For a compound material, consisting of a number n_i of N distinct elements i, the electronic density is extended from eq. (2) as:

$$\rho_e = \frac{\sum_{i=1}^{N} n_i Z_i}{\sum_{i=1}^{N} n_i A_i}\rho. \tag{3}$$

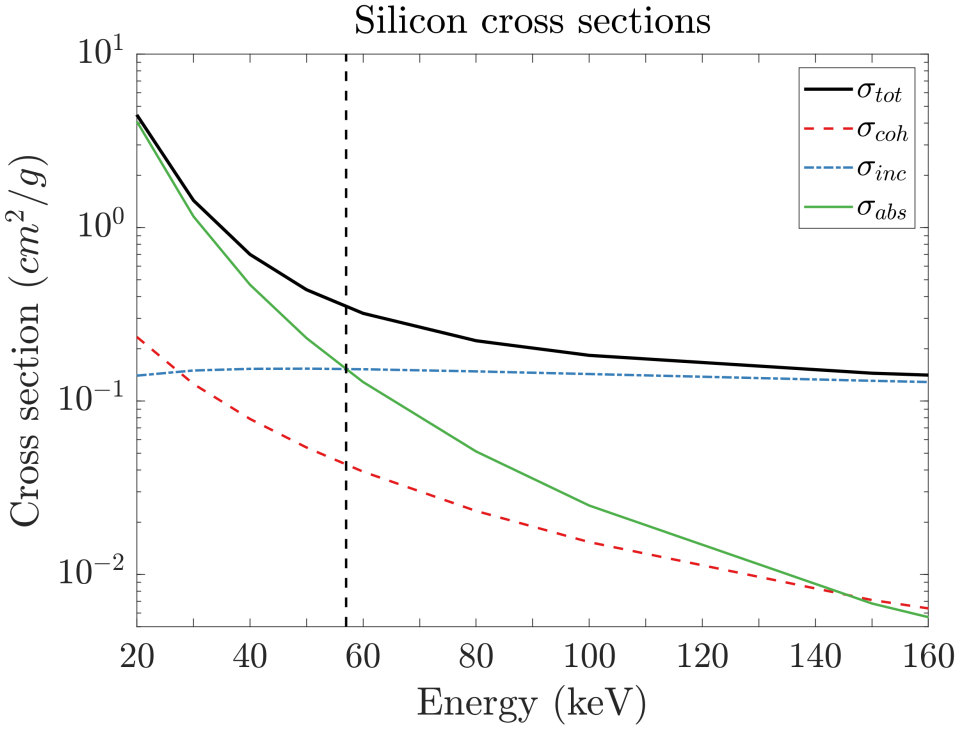

Figure 1: The NIST cross sections look-up tables, exemplified for silicon. The total cross section (solid black), is the sum of the individual photoelectric absorption (solid green), coherent (dashed red) line and incoherent scattering (dash-dotted blue) cross sections. The vertical dashed black line near 60 keV denotes the intersection between σ_{abs} and σ_{inc}. Note the logarithmic scale in the $y-$axis.

To approximate the atomic number of such a compound we use the definition of effective atomic number, Z_e, presented by Azevedo et al. [4] defined as a non-integer atomic number that corresponds to an artificial element, for which the interactions are assumed to be modeled by the X-ray attenuation cross sections. The cross sections for the artificial element Z_e are obtained by a linear interpolation between the cross section of the two adjacent elements in the periodic table:

$$\sigma_e(Z_e, E) = (1 - \epsilon)\sigma_e(Z', E) + \epsilon\sigma_e(Z' + 1, E). \tag{4}$$

Therein, Z' is the lower adjacent element $Z' = floor(Z)$ and ϵ is the difference $\epsilon = Z' - Z$.

In terms of the effective atomic number and electronic density presented above, we express the LAC of a material m as:

$$\mu^m(E) = \rho_e^m \sigma_e(Z_e^m, E). \tag{5}$$

Investigated materials are tabulated in Table 1. The material properties were calculated from their respective measured bulk densities ρ using the paper by Bond et al.[13]. Note that a set of materials was scanned simultaneously within a carousel[14], while a set of other materials, with larger diameter or attenuation were scanned individually. The material features listed in Table 1 will be considered as the ground truth for the remainder of the paper.

Table 1: All the materials composing the samples and their respective physical properties. Note that the values of Z_e were calculated with ZeCalc [13], setting the kV to 160 kV. Measurement uncertainties were ±0.15% for ρ, leading to uncertainties of about ±0.5% for ρ_e and Z_e. The density measurement were taken from [4] as the same materials were used. †Materials placed in the six samples carousel. ‡Materials scanned individually.

Material	**Formula**	**Diameter** (mm)	ρ (g/cm^3)	ρ_e (e^-mol/cm^3)	Z_e
‡Graphite A	C	50	1.70	0.846	6
†Graphite B	C	12.7	1.85	0.924	6
†POM	$(CH_2O)_n$	12.7	1.40	0.749	7.01
†Water	H_2O	12.7	1.00	0.554	7.45
†PTFE	$(C_2F_4)_n$	12.7	2.17	1.042	8.43
†Magnesium	Mg	12.7	1.74	0.857	12
‡Aluminum	Al	25	2.699	1.300	13
†Silicon	Si	12.7	2.33	1.162	14
‡Titanium	Ti	12.7	4.540	2.085	22

2.2. MultiX ME 100 V2 detector array

The MultiX ME 100 V2 consists of a linear array of CdTe-based photon-counting X-ray detectors capable of recording energies from 20 to 160 keV in 1.1 keV energy bin increments, maximum number of energy bins $N_E = 128$. Optionally, for custom applications, two to six independently tunable energy bins can be specified within the full energy range. In this alternative mode, bins can be separated by a gap or they can overlap. Each module consists of 4 continuous pixelated CdTe crystals approximately 2.5 cm in length. Each crystal is divided into 32 detector elements. Each detector element is $3-$ mm thick, $0.8-$ mm wide and $0.8-$ mm high. Up to 20 modules can be daisy-chained to form a $200-$ cm linear detector array. An interface board connected to a host computer acquires and transfers the data from the modules via an Ethernet link. The detectors can have integration times from 0.5 ms to 100 ms (in 10 μs increments). MultiX ME100 V2 is a pulse-counting detector, thus each count measured in the image refers to one detected photon. The energy resolution of the detector under high X-ray fluxes is of 6.5% (8 keV) at 122 keV. A lead collimator built into the module and surrounding the detector elements provides some X-ray collimation and radiation shielding. To implement a robust experimental tool, an enclosure was designed to hold and align, as well as safely store and transport, the detector modules.

For system control and acquisition of the MultiX radiography and CT data, we developed an automated software utility. The manufacturer provided an Application Programming Interface (API) to enable control of the detector array that was then incorporated into the software. To accommodate the need for computed tomography capabilities, the software was designed to control a Newport XPS motion controller driving a rotary stage (Newport Corporation, Irvine, California). An API from Newport was used to interface the software with the motion controller. Individual digital line radiographs using selected integration times can be acquired and saved in a raw binary file format. The software allows for a computed tomography scan over a selected angular range and integration time to be automatically acquired and saved for later analysis.

2.3. Experimental setup

An YXLON 450-D11 (YXLON International, Hudson, Ohio) X-ray source was used with an acceleration voltage of 160 kV, anode filament current of 0.5 mA and 1 mm focal spot. The spectrum was filtered with 2 mm of aluminum. The detector was made up of two linear array PCD MultiX ME100 modules. For all the SCT scans performed in this work 360 projections were acquired, by rotating the sample stage at 1° increments. For each projection, the total exposure time was set to 5 s. The source to detector distance (SDD) was set to 3000 mm whereas the source to sample distance (SOD) was set to 2830 mm.

2.4. Correction steps

The raw data collected by photon counting detectors is distorted by physical interactions such as charge sharing, weighting potential, escape peaks, pulse pile-up and insufficient charge collection [14, 15, 16, 17, 18]. These effects lead to a skewing of the measured spectrum from the central energies towards low- and high-energy tails. Since these effects are energy and flux dependent, different samples yield different distortions, and hence, errors in their LAC retrieval. To correct for these distortions, we employ a correction algorithm presented by Dreier et al. [19]. In contrast to other algorithms, this approach is flux dependent and fast (milliseconds per pixel), making it a suitable candidate for applications with high throughput demand. A plot of the X-ray source spectrum, before and after the correction has been applied is shown in Fig. 2.

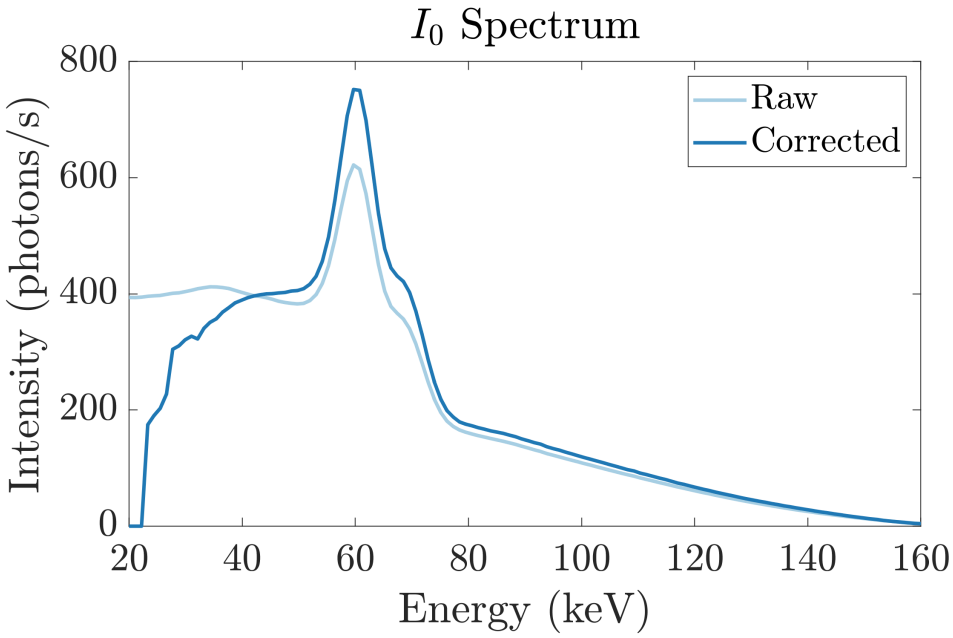

Figure 2: The raw (solid light blue) and spectral corrected (solid dark blue) X-ray source spectra, as measured by the MultiX ME100. The mean flux density per pixel was approximately 26000 Photons $\cdot$ s^{-1}/pixel. Note that for this flux density the pile-up effect is not visible in the spectra but appears in the measured LAC (see Fig. 4).

Another relevant source of distortions in data acquisition is the radiation scattered by the sample and the environment. Low angle scattered photons which do not escape the detectors contribute to the transmitted radiation in Lambert-Beer's law resulting in a lowering of the measured

LAC. The effect in the reconstructed volumes is a global loss of contrast between different materials and can lead to severe cupping artifacts. The influence of the scattered radiation on the acquisition depends on the size of the detectors and samples, material composition of the sample and the distance between the sample and the detectors. Lastly, it depends on the source spectrum and the materials' scattering cross sections. In an SCT acquisition, where the source's potential is typically set up to 160 kV, scattering becomes the dominant interaction of high-energy photons (see Fig. 1), lowering the attenuation measured at the high-energy bins of the PCD. It is therefore important to adopt methods to suppress X-ray scattering. In this work, the X-ray scattering was estimated using a deep learning convolutional neural network (CNN) introduced by Maier et al. [20]. The training datasets were obtained with a Monte Carlo (MC) simulation framework for scattering estimates presented by Busi et al. [21] A random sample generator was created with the aid of a software tool presented by Kazantsev et al. [22], to reproduce artificial samples composed of different materials. In contrast with the gold standard MC simulation, once trained, the CNN can provide scattering estimates in a few hundreds of milliseconds, while MC simulations usually take at least several minutes to converge, depending on the desired resolution. Note that the environmental X-ray scattering is not included in the model.

2.5. LAC volume reconstruction and energy selection

After the spectral and scattering corrections are performed on the spectra of each projection of the CT scan, the data is rebinned from $N_E = 128$ energy bins into $N_E = 64$ to increase photons statistics of each energy bin, while preserving flexibility in the energy selection and spectral resolution. The merging is done by summing the radiation I detected in pairs of adjacent energy bins as follows:

$$I^{E'_k} = I^{E_{2k-1}} + I^{E_{2k}}, \quad k = 1, ..., 64. \tag{6}$$

The energy values assigned to the new energy bins E'_k are calculated by taking the weighted mean according to the source spectrum as follows:

$$E'_k = \frac{I_0^{E_{2k-1}} \cdot E_{2k-1} + I_0^{E_{2k}} \cdot E_{2k}}{I_0^{E_{2k-1}} + I_0^{E_{2k}}}, \quad k = 1, ..., 64. \tag{7}$$

Therein, I_0 is the corrected flat-field measurement, i.e. the projection without the sample being inserted, and corresponds to the source spectrum as measured by the detectors, also referred as the system's spectral response. We note that the merging procedure similarly can be done for a power of 2 of new energy bins (i.e. $N_E = 1, 2, 4, 8, 16, 32$). For the remainder of the paper we denote the new energy bins as $E_k \equiv E'_k$, for practical reasons.

The energy resolved projections I are converted to linear attenuation coefficients, μ, using the Lambert-Beer's law:

$$\mu^{E_k}(\vec{x}) = -log\frac{I^{E_k}(\vec{x})}{I_0^{E_k}(\vec{x})}, \quad k = 1, ..., 64; \tag{8}$$

where $\vec{x}$ is the detector pixel array. Note that in this work we perform 2D slice reconstructions with fan-beam collimation since the detector is a linear array. The slice reconstructions are performed individually for each energy bin using the Filter Back Projection (FBP) routines included in Livermore Tomography Tools, a software package developed at LLNL[23]. An example of the slice reconstructions at four different energies is shown in Fig. 3. The reconstruction at $E_k = 27.3$ keV shows strek artifacts induced by photon starvation from the high attenuation of silicon at low energies. We also note that the contrast between the different materials varies

as a function of energy. For example, the contrast between graphite and magnesium is higher at 44.8 keV than 139.6 keV, whereas the opposite behavior is found in the contrast between graphite and POM.

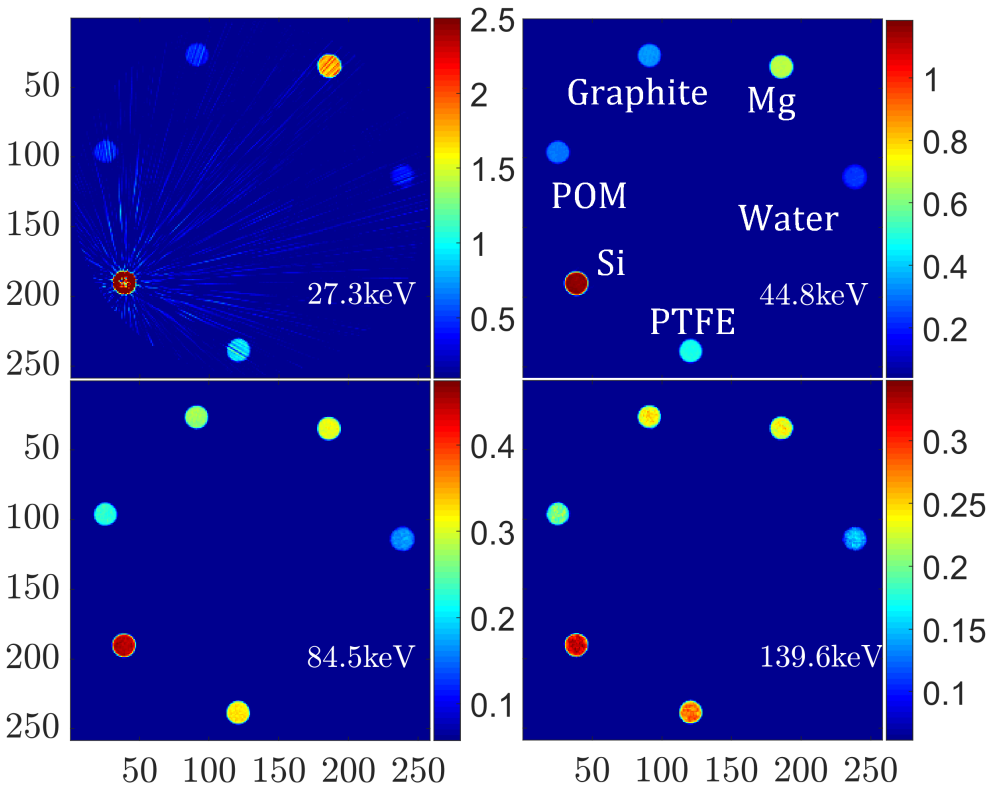

Figure 3: Four individual energy LAC resolved slice reconstructions of the materials in the carousel, at the energies $E_k = 27.3, 44.8, 84.5, 139.6$ keV. The axes' unit corresponds to the pixel size (0.8 mm). The scale unit is the linear attenuation (cm^{-1}).

For each material, the LAC mean value and standard deviation within a region of interest (ROI) are calculated for each energy resolved reconstruction. In Fig. 4, we show an example of silicon's LAC measured with and without the correction steps discussed in Section 2.4, as well as the corresponding ground truth. The correction algorithm helps correct the LAC towards the ground truth values at the low energies, where the contrast between organics compounds (e.g. PTFE and POM) is highest. The error increases towards the low- and high-energies due to spectral distortions, which cannot be completely restored by the correction algorithms. At certain energies, the LAC values deviate from the expectation due to complete attenuation of the radiation by the sample, resulting in photon starvation. To estimate the ρ_e and Z_e of each material, the method requires an automated selection of the low- and high-energy thresholds, E_i and E_f, which correspond to energy thresholds that exclude bins in which the LAC is affected by low photon statistics and pulse pile-up. For all the materials scanned in this work, these two

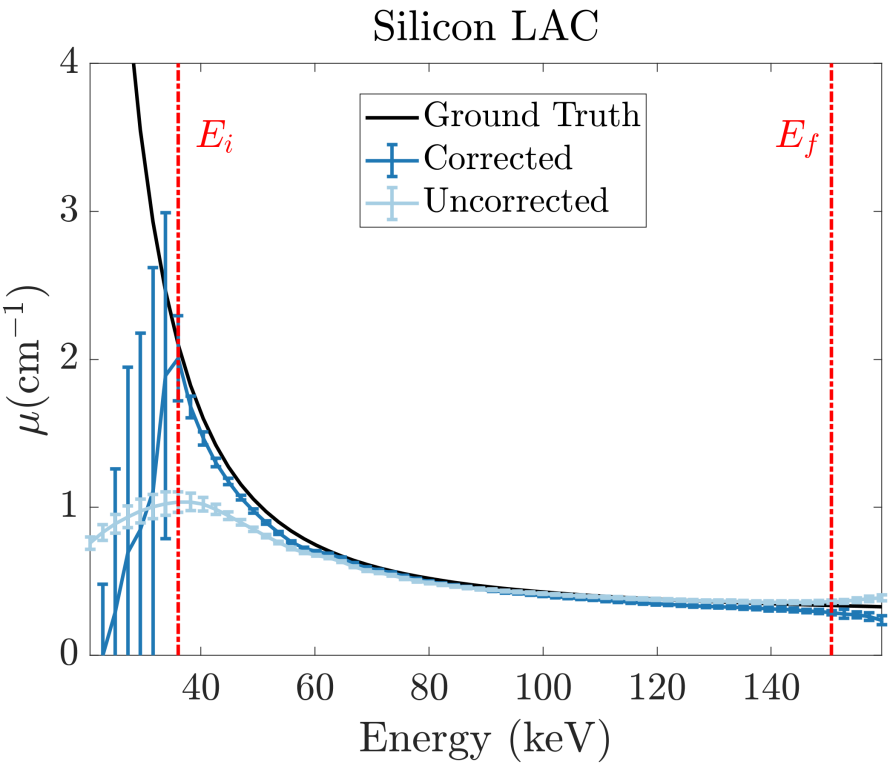

Figure 4: Energy resolved LAC, exemplified for Silicon. The solid black line is the ground truth obtained by using the ground truth values of ρ_e and Z_e in Table 1, using NIST cross-sections. The dark and light blue lines are the ROI mean LAC calculated as described in Section 2.5, with and without the correction steps of Section 2.4 being applied respectively. The error-bars represent the respective standard deviation values. The vertical red dash-dotted lines are the low- and high-energy thresholds E_i and E_f found by the energy selection step given in Section 2.5.

thresholds were calculated by assuming the LAC to be monotonically decreasing, and with no inflection points in the incoherent scattering regime ($E > 60$ keV). This assumption is useful, in case of a PCD, for materials (i.e. $1 \leqslant Z_e \leqslant 42$) that do not have a K-edge within the detector's energy range. For MultiX ME100 that is between 20 and 160 keV. The low-energy threshold E_i is determined by taking the first derivative of the estimated LAC ($\delta\mu(E)/\delta E$) and locating the nearest zero intercept closest to the lowest-energy bin, as it corresponds to a relative maximum with a change from increasing to decreasing. The high-energy threshold E_f is determined by taking the second derivative of the estimated LAC ($\delta^2\mu(E)/\delta E^2$), and locating the bin nearest the zero intercept, closest to the highest energy bin, as it corresponds to an inflection point. The determination of the energy thresholds is illustrated in Fig. 4 for silicon.

2.6. Spectral ρ_e/Z_e Estimation (SRZE)

We introduce a method that estimates the physical properties (ρ_e and Z_e) of a material from its corrected LAC measurements. The estimation is performed by solving a constrained minimization of a cost function $g(E)$:

$$\arg\min g(E). \tag{9}$$

We define the cost function $g(E) = |\tilde{\mu}(E) - \mu(E)|^2$, as the squared distance between the measured LAC, $\tilde{\mu}(E)$, and its relative theoretical definition $\mu(E)$, parametrized by ρ_e and Z_e as in eq. (5). Therefore, for a spectral acquisition eq. (9) becomes:

$$\underset{\{\rho_e, Z_e\}}{\arg\min} \sum_{k=i}^{f} \lambda_{E_k} |\tilde{\mu}(E_k) - \rho_e \sigma_e(Z_e, E_k)|^2. \tag{10}$$

Therein, λ_{E_k} are the energy weights, computed as the reciprocal of the variance (s^2) of each material's LAC in their ROI, $\lambda_{E_k} = 1/s^2(\tilde{\mu}_{E_k})$. These can be interpreted as the weight given to each energy bin E_k into the estimation of the material's features. Note that the summation runs from the low- and high-energy thresholds E_i and E_f, found as described in the previous section. The minimization process in this work was performed with MATLAB®'s routine function FMINCON with solution boundaries $\rho_e = 0 - 15$ e$^-$mol/cm^3 and $Z_e = 1 - 99$ and initial guesses $\rho_e^0 = 1$ e$^-$mol/cm^3 and $Z_e^0 = 7$. No particular dependency on the starting values was observed. Note that in the case of materials presenting a K-edge in the attenuation coefficients, the energy bins below the edge would be truncated making it compatible with estimation method, however none of the materials presented here have a K-edge within the energies in the PCDs range.

3. Results and discussion

In this section we present the experimental results obtained with the SRZE method presented in Section (2.6), for all the materials scanned (see Table 1). The accuracy of the estimation is calculated as the percent relative deviation from the ground truth for the effective atomic number as:

$$\Delta Z_e^{rel} = 100\% \cdot \frac{Z_e^{est} - Z_e^{gt}}{Z_e^{gt}}, \tag{11}$$

and similarly, for the electron density by substituting Z_e with ρ_e, where superscripts *est* and *gt* refer to estimated and ground truth, respectively. The ground truth values for the material features are listed in Table 1. All the results are plotted in Fig. 5 and listed with comparisons to the results reported in a previous study[24] in Table 2.

3.1. Discussion of Results

The accuracy of the SRZE method in Fig. 5 and Table 2 shows promising results in the calculation of the effective atomic number, with an overall mean relative error value of 1.79%. It is observed that the estimation of Z_e worsens for smaller Z_e, due to lower performance of the detector in terms of spectral resolution at the lower-energy bins and lower contrast between LAC curves of adjacent Z_e values. Moreover, the spectral distortions in the low-energy reconstructions lead to higher standard deviations, and hence less energy weight λ_{E_k} in the estimation method. However, the highest contrast of low-Z_e materials is found at lower energies.

The estimation of ρ_e on the other hand shows a 4% negative bias in the mean relative error value, perhaps due to an overall underestimation of the measured energy resolved attenuation coefficient, also visible in Fig. 4. One reason for this may be due to a high amount of environmental X-ray scattering, not considered in the analysis. For these experiments, except for the titanium, aluminum, and graphite A scans, the source was not collimated into a fan-beam geometry and a large portion of the beam hit the sample stage, mostly composed of metal parts. The small distance between the sample stage and the detector permitted a large portion of the environmental

scattering to reach the detectors. The large error in the estimation of silicon's electron density (ρ_e) may be due to the use of monocrystalline silicon, which is known to exhibit a different X-ray cross section than polycrystalline silicon[4, 24]. The results are comparable to the ones reported in a previous work using state-of-the-art Dual-Energy CT[24], besides the significant lower performance on the estimation of ρ_e, which is due to the reasons discussed above.

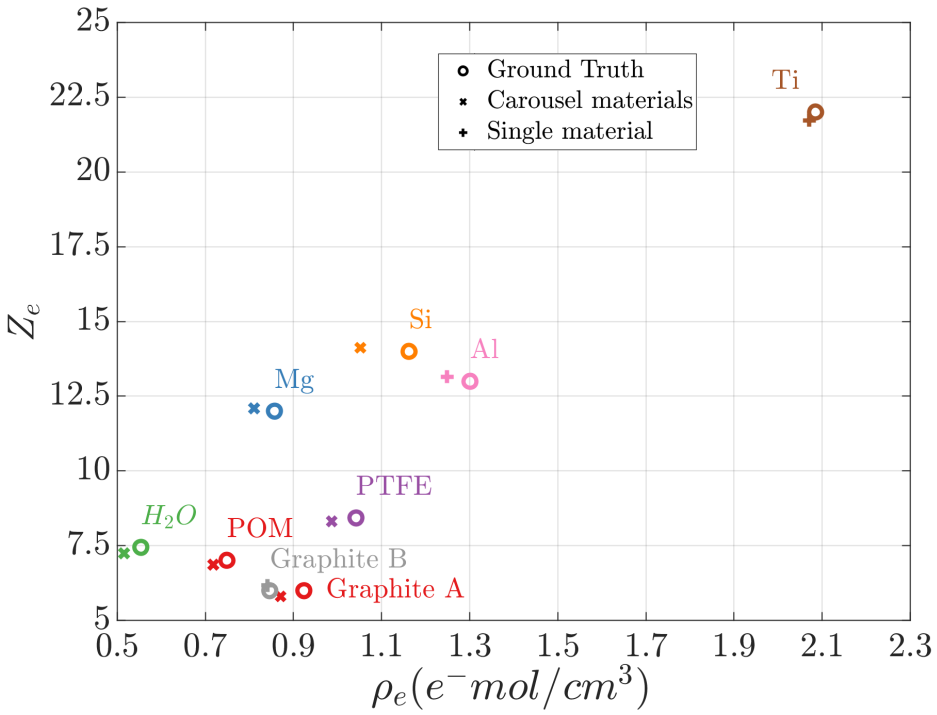

Figure 5: Scatter plot of the ρ_e, Z_e results obtained using the SRZE method.

3.2. Energy Selection Analysis

To test the robustness and sensitivity of the E_i and E_f thresholds selection procedure described in Section 2.5 we ran the SRZE estimation method over a range of values of the low- and high-energy thresholds E_i and E_f. Fig. 6 shows the relative percent deviation of the estimated material features for aluminum. Note that the diagonal elements correspond to taking only two adjacent energy bins and the values below the diagonal are not calculated as they have no physical representation. The thick dark areas show that the key factor for accurate estimation of the LAC, and thus ρ_e and Z_e is the selection of the low-energy threshold E_i. The optimal performance is reached by truncating the low-energy bins, for which the spectral distortions and photon starvation cause a distortion of the measured LAC. On the other hand, choosing a higher threshold for the low-energy bins yields a poor estimation, as the bulk of the material properties is revealed by the low energy bins.

It is also shown in Fig. 6 that the selection of the high-energy threshold E_f has less impact on the estimation of the LAC, and thus ρ_e and Z_e. The large areas in which the accuracy is below

Table 2: SRZE estimation of the material's features. SIRZ-2 values reported are taken from [24]. The SIRZ-2 results for titanium are unpublished. †Materials placed in the six samples carousel. ‡Materials scanned individually. *The mean values were calculated from the absolute values of each column.

Material	ρ_e^{gt} (e^-mol/cm^3)	**SRZE** $\rho_e^{rel}(\%)$	**SIRZ-2** $\rho_e^{rel}(\%)$	Z_e^{gt}	**SRZE** $\Delta Z_e^{rel}(\%)$	**SIRZ-2** $\Delta Z_e^{rel}(\%)$
‡Graphite A	0.85	-0.5	0.3	6	2.9	0.5
†Graphite B	0.92	-5.7	1.5	6	-3.2	-0.8
†POM	0.75	-4.2	0.3	7.0	-2.0	-1.3
†Water	0.55	-6.9	-0.2	7.4	-2.7	-0.4
†PTFE	1.04	-5.3	-0.1	8.4	-1.3	-1.1
†Magnesium	0.86	-5.4	-0.2	12	0.8	-0.4
‡Aluminum	1.30	-3.2	1.8	13	0.7	-2.0
†Silicon	1.16	-9.5	-0.5	14	0.8	-4.4
‡Titanium	2.08	-0.7	-	22	-1.2	-
*Mean	-	4.6	0.6	-	1.7	1.4

2% indicate that the estimation method is overdetermined and there may be a material dependent optimal choice of the energy bins, that would lead to optimized results. The difference, in shape, between the dark areas for ρ_e and Z_e, suggests that there may be an optimized choice of energy bins for an independent estimation of ρ_e and Z_e.

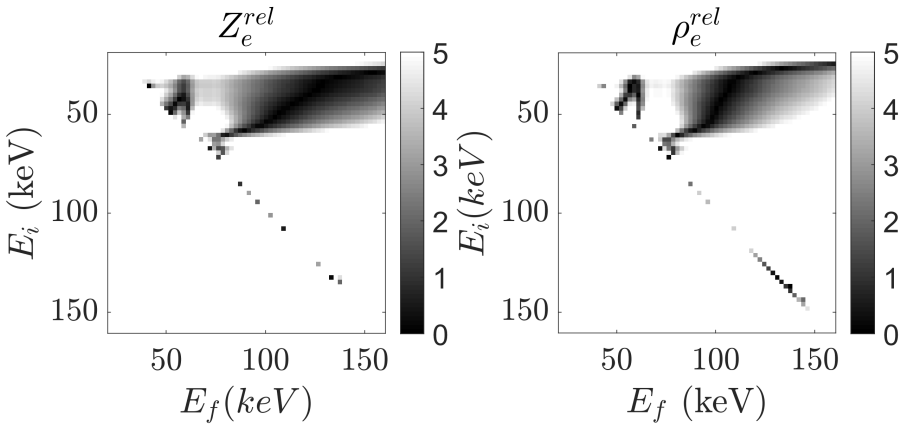

Figure 6: Plot of the material features estimation accuracy as a function of the E_i and E_f thresholds, exemplified for aluminum. The scale unit is the percent relative deviation (%) expressed in eq. (11).

4. Conclusions

We have presented a method for the estimation of system-independent physical properties of materials, from Spectral CT measurements. In contrast to other methods, this does not require

a calibration step using reference materials and can be used with any number of energy bins. However, it relies on the accurate measurement of the energy dependence of the attenuation coefficients. We found the method to be more robust to the variety of material samples using 64-energy bins, followed by a detection and truncation of the low- and high-energy bins where the spectral distortions cannot be fully corrected. Our assumption for the selection of the energy bin thresholds is supported by the physical properties of the attenuation coefficients of materials not presenting a K-edge, however the method is expected to be able to operate in this condition as well. The accuracy results are comparable to the ones obtained with the state-of-the-art techniques employing dual-energy CT scans, while our method is done with a single scan and it has a better performance for highly attenuating materials. Photon counting detectors are still under development therefore, improvements in the detector's response will lead to a better estimation of the material's features. Further experiments will test the robustness of the method to materials with larger range of effective atomic number Z_e, and presence of K-edges. Additional experiments will test the precision and accuracy of the method using different scanning parameters such as source potential, filament current and different source filters as well as better environmental X-ray scattering reduction.

Acknowledgments

The author would like to thank Innovation Fund Denmark for funding the project. The authors also acknowledge Bill Brown and Brian Fix (LLNL) for their efforts in the early implementations of the MultiX ME100 hardware and software in the CT scanning system.

[1] H. E. Martz, C. M. Logan, D. J. Schneberk, P. J. Shull, X-ray Imaging: fundamentals, industrial techniques and applications, CRC Press, 2017.

[2] Z. Ying, R. Naidu, C. R. Crawford, Dual energy computed tomography for explosive detection, Journal of X-ray Science and Technology 14 (4) (2006) 235–256.

[3] K. Wells, D. Bradley, A review of X-ray explosives detection techniques for checked baggage, Applied Radiation and Isotopes 70 (8) (2012) 1729–1746.

[4] S. G. Azevedo, H. E. Martz, M. B. Aufderheide, W. D. Brown, K. M. Champley, J. S. Kallman, G. P. Roberson, D. Schneberk, I. M. Seetho, J. A. Smith, System-independent characterization of materials using dual-energy computed tomography, IEEE Transactions on Nuclear Science 63 (1) (2016) 341–350.

[5] A. S. Wang, D. Harrison, V. Lobastov, J. E. Tkaczyk, Pulse pileup statistics for energy discriminating photon counting x-ray detectors, Medical physics 38 (7) (2011) 4265–4275.

[6] H. Ding, S. Molloi, Image-based spectral distortion correction for photon-counting x-ray detectors, Medical physics 39 (4) (2012) 1864–1876.

[7] P. M. Shikhaliev, Energy-resolved computed tomography: first experimental results, Physics in Medicine & Biology 53 (20) (2008) 5595.

[8] V. Rebuffel, J. Rinkel, J. Tabary, L. Verger, New perspectives of X-ray techniques for explosive detection based on CdTe/CdZnTe spectrometric detectors, Proc. of the Int. Symp. on Digital Industrial Radiology and Computed Tomography 2.

[9] K. C. Zimmerman, E. Y. Sidky, T. G. Schmidt, Experimental study of two material decomposition methods using multi-bin photon counting detectors, Medical Imaging 2014: Physics of Medical Imaging 9033 (2014) 90333G.

[10] A. Brambilla, P. Ouvrier-Buffet, J. Rinkel, G. Gonon, C. Boudou, L. Verger, CdTe linear pixel x-ray detector with enhanced spectrometric performance for high flux x-ray imaging, IEEE Transactions on Nuclear Science 59 (4) (2012) 1552–1558.

[11] A. Brambilla, A. Gorecki, A. Potop, C. Paulus, L. Verger, Basis material decomposition method for material discrimination with a new spectrometric x-ray imaging detector, Journal of Instrumentation 12 (08) (2017) P08014.

[12] C. T. Chantler, Theoretical form factor, attenuation, and scattering tabulation for Z= 1–92 from E= 1–10 eV to E= 0.4–1.0 MeV, Journal of Physical and Chemical Reference Data 24 (1) (1995) 71–643.

[13] K. Bond, J. Smith, J. Treuer, S. Azevedo, J. Kallman, H. Martz, ZeCalc algorithm details, version 6, Tech. rep., LLNL Tech. Rep., LLNL-TR-609327,(Jan. 2013). To request a copy of ZeCalc software, contact Mary Holden-Sanchez at holdensanchez2@ llnl. gov (2013).

[14] A. A. Dooraghi, B. J. Fix, J. A. Smith, W. D. Brown, S. G. Azevedo, H. E. Martz, Characterization of a spectroscopic detector for application in x-ray computed tomography, in: Developments in X-Ray Tomography XI, Vol. 10391, International Society for Optics and Photonics, 2017, p. 103911G.
[15] P. Guerra, A. Santos, D. Darambara, Development of a simplified simulation model for performance characterization of a pixellated CdZnTe multimodality imaging system, Physics in Medicine & Biology 53 (4) (2008) 1099.
[16] R. H. Redus, J. A. Pantazis, T. J. Pantazis, A. C. Huber, B. J. Cross, Characterization of CdTe detectors for quantitative X-ray spectroscopy, IEEE Transactions on Nuclear Science 56 (4) (2009) 2524–2532.
[17] J. Cammin, J. Xu, W. C. Barber, J. S. Iwanczyk, N. E. Hartsough, K. Taguchi, A cascaded model of spectral distortions due to spectral response effects and pulse pileup effects in a photon-counting x-ray detector for CT, Medical physics 41 (4).
[18] J. Plagnard, Comparison of measured and calculated spectra emitted by the X-ray tube used at the gustave roussy radiobiological service, X-Ray Spectrometry 43 (5) (2014) 298–304.
[19] E. S. Dreier, J. Kehres, M. Khalil, M. Busi, Y. Gu, R. Feidenhans, U. L. Olsen, Spectral correction algorithm for multispectral CdTe x-ray detectors, Optical Engineering 57 (5) (2018) 054117.
[20] J. Maier, S. Sawall, M. Knaup, M. Kachelrieß, Deep Scatter Estimation (DSE): Accurate real-time scatter estimation for X-Ray CT using a Deep Convolutional Neural Network, Journal of Nondestructive Evaluation 37 (3) (2018) 57.
[21] M. Busi, U. L. Olsen, E. B. Knudsen, J. R. Frisvad, J. Kehres, E. S. Dreier, M. Khalil, K. Haldrup, Simulation tools for scattering corrections in spectrally resolved x-ray computed tomography using McXtrace, Optical Engineering 57 (3) (2018) 037105.
[22] D. Kazantsev, V. Pickalov, S. Nagella, E. Pasca, P. J. Withers, TomoPhantom, a software package to generate 2D–4D analytical phantoms for CT image reconstruction algorithm benchmarks, SoftwareX 7 (2018) 150–155.
[23] K. Champley, Livermore tomography tools (LTT) technical manual, LLNL-SM-687016, pages 1-165, 2016.
[24] K. M. Champley, S. G. Azevedo, I. M. Seetho, S. M. Glenn, L. D. McMichael, J. A. Smith, J. S. Kallman, W. D. Brown, H. E. Martz, Method to extract system-independent material properties from dual-energy X-ray CT, IEEE Transactions on Nuclear Science 66 (3) (2019) 674–686.